Chapter-3 Reduced Graphite Oxide and MoS_2 Based Electrodes for Hydrogen Generation

3.1 Introduction

Consumption of fossil fuels as energy source causes damaging environmental issues and global warming. Therefore, it is critical to develop efficient renewable energy generation systems to fulfil growing energy demand of society. In this regard, molecular hydrogen gas (H_2) has been advocated as one of the most promising clean and sustainable energy sources for ecological system with a very high calorific value along with nearly zero emission of hazardous gases [1,2]. Hydrogen does not generally exist in the free state rather it occurs in compounds such as hydrocarbons and water. At present in the industrial market natural gas steam reforming is predominantly used for hydrogen production but these processes release CO_2 into the atmosphere, thereby compromising the environmental benefits of using H_2 as a fuel. So, long-term economic and industrial production of hydrogen is a daunting challenge. In this context, hydrogen production via electrolysis generates 99.99% pure hydrogen compared to any other production method [126]. The typical schematics for decomposition of water into hydrogen and oxygen is shown in **Figure 3.1**. This method has gained incredible attention because of its cost effectivity, high efficiency, and environmentally friendly response as it does not produces no carbon dioxide. However, electrochemical process of hydrogen evolution reaction (HER) must overcome an activation energy barrier, referred as overpotential (η) in electrochemistry. They frequently require the use of electrocatalysts to reduce the value of η and, as a result, increases the reaction rate and efficiency [127].

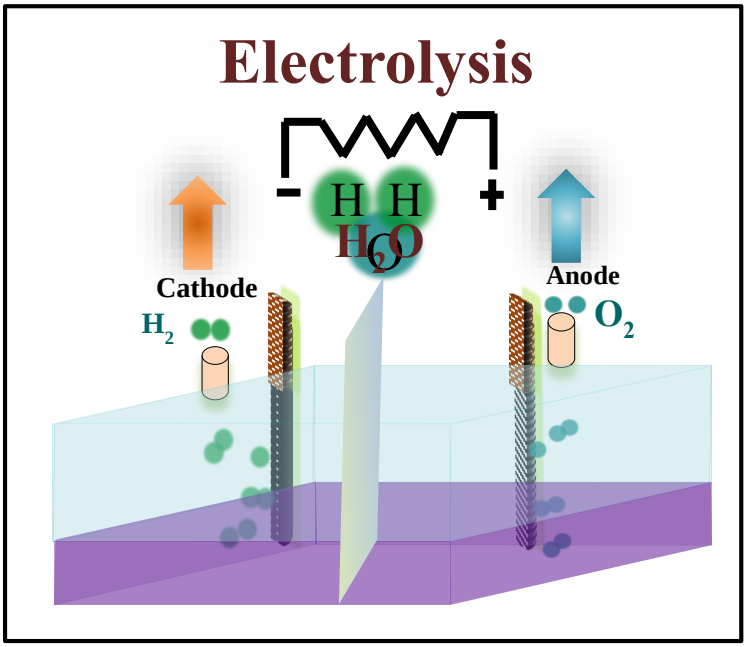

Figure 3.1 *Schematic representation of electrolysis of water.*

So far, the Pt-based nanomaterials are known as the most proficient electrocatalyst for HER due to their high efficiency and smaller overpotential, but the earth scarcity and high cost restrict their large-scale application or industrialization [128,129]. As a result, finding low-cost, plentiful, high-efficiency, and environmentally benign catalytic cathode materials has become a major challenge. In this context, extensive investigation for electrocatalyst is being done to develop more sustainable and cost-effective catalysts for HER, such as metal oxides, metal carbides, metal dichalcogenides, metal phosphides etc [130–134]. In general, pristine carbon nanostructures are not known as good electrocatalyst for HER, however, their surface modification can yield better electrocatalysts. Among metal dichalcogenides, MoS_2 nanostructures are being explored as a potential noble metal free and non-polluting electrocatalyst for HER due to its natural abundance, high acidic stability and excellent electrochemical activity [135, 136]. Electrocatalytic performance of bulk MoS_2 is hindered by its low intrinsic conductivity and ease of aggregation. The maximum catalytic performance of MoS_2 could be achieved by large exposure of edge sites of unsaturated sulphur atoms compared to its

basal plane [137]. The ultrathin layers in nanostructured MoS_2 may provide large surface area and electrochemical active sites, suitable for electrochemical energy generation and storage device.

In order to get maximum active edge sites for catalytic activity, different morphologies of MoS_2 nanostructures have been investigated [138-140]. Cui and co-workers developed edge rich vertically aligned MoS_2 films and showed higher a Tafel slope of 105-120 mV dec^{-1} at voltage scan rate of 2 mV sec^{-1} suggesting lower catalytic activity for HER [141]. Jaramillo's group reported a highly ordered 3D porous MoS_2 structure with preferentially exposed active edge sites for improvement of HER performance with a Tafel slope of 50 mV dec^{-1} at 5 mV s^{-1} [142]. Wang *et al.* showed a Tafel slope of 109 mV dec^{-1} by activating sulfur edges in Fe, Co, Cu doped MoS_2 [143]. Wang *et al.* synthesized mechanical activated MoS_2 flakes via high-energy ball milling process and obtained a Tafel's slope around 104 mV dec^{-1} with low current density of 0.9 mA cm^{-2} at over-potential of 0.200 V [144]. The aforementioned results support good catalytic activity of MoS_2 nanostructure towards HER but unfortunately these methods have a high level of technical complexity and lacks scalability, which limits their utility in practical applications. In the present work, we have investigated the electrochemical activity of hydrothermally prepared rGO samples (rGO-HH and rGO-Urea), hexagonal phase of MoS_2 nanostructures (nanocluster, nanosheets and nanoflowers) and MoS_2-rGO heterostructure as cathode material electrodes for HER study.

3.2 Fundamentals of HER

The overall water splitting reaction in acidic conditions is described by **equation 3.1**-

$$\boldsymbol{H_2O \rightleftharpoons H_2 + \frac{1}{2}O_2} \qquad (3.1)$$

Under the ambient pressure and temperature condition, the Gibbs free energy and enthalpy of the water splitting reaction are 237.2 and 286 kJ mol^{-1}, respectively [145]. The Gibbs free energy is converted into the standard cell potential using succeeding **equation 3.2**-

$$\boldsymbol{\Delta G^{0} = -nFE^{0}} \quad (3.2)$$

where, n represents number of electrons transferred per product formed, F is the Faraday constant and E° represents the standard cell voltage. The reversible voltage is computed as 1.23 V, which is the thermodynamic potential required for splitting of water. The reaction can be divided into two half-cell reactions: the cathodic half-cell reaction (**equation 3.3 and 3.4)** where the proton reduction or HER occurs and anodic half-cell reaction (**equation 3.5 and 3.6)**, where the occurrence of water oxidation reaction or OER happens.

Cathode:

$$\boldsymbol{2H^{+} + 2e^{-} \rightleftharpoons H_2}\ \textbf{, with } \mathbf{E^0 = 0} \quad (3.3)$$

$$\boldsymbol{E = E^{0} + \frac{0.059}{2} log\,[H^{+}]^{2} = E^{0} + 0.059\, log[H^{+}] = 0 - 0.059\, pH} \quad (3.4)$$

Anode:

$$\boldsymbol{H_2O \rightleftharpoons 2H^{+} + \frac{1}{2}O_2 + 2e^{-}} \qquad \textbf{with } \mathbf{E^0 = 1.23} \quad (3.5)$$

$$\boldsymbol{E = E^{0} + \frac{0.059}{4} log\,[H^{+}]^{4} = E^{0} + 0.059\, log[H^{+}] = 1.23 - 0.059\, pH} \quad (3.6)$$

The overall water splitting curve (I-V characteristics) is shown in **Figure 3.2**.

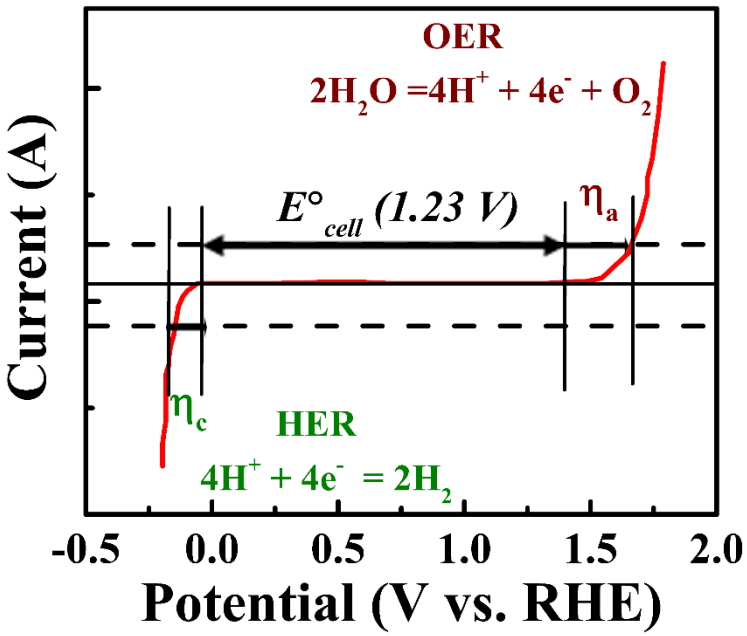

Figure 3.2 *Current vs. potential (I–V) graph for electrolysis of water.*

Further, the influence of the pH on the potential can also be considered using **equation 3.4** and **equation 3.6** [145–147]. For each half-reaction, the Nernst equation shows that redox potentials shift linearly by -59 mV for every pH unit. Electrochemical reactions, on the other hand, frequently require more energy than thermodynamics dictate. The true value applied to the electrolyser is always greater, and this is known as overpotential (difference between the equilibrium potential and applied potential). The cathode and anode materials, as well as other resistances involved with the electrolytic cell design, all have a direct impact on driving potential of HER as illustrated in following **equation 3.7** [148]-

$$\boldsymbol{E = 1.23 + iR + \eta} \qquad (3.7)$$

Here, iR is the ohmic potential drop induced by the current flow in electrolytes and η is the reaction overpotential, one of the most essential electrode metrics to measure its electrochemical performance. The smaller overpotential and larger current indicate the higher efficiency of electrode for HER. As another important electrochemical parameter, Tafel slope reflects the intrinsic catalytical activity of a catalyst [149]. The value of Tafel slope can be obtained from the polarization curves using following Tafel **equation 3.8**-

$$\eta = b\,log j + a \tag{3.8}$$

where j is the current density (mA cm^{-2}) and the Tafel's slope (b) is an inherent property of the catalyst determined by the HER rate limiting step. The smaller value of Tafel slope suggests better HER activity and hence the electrocatalysts performances are compared based on low Tafel slope values.

3.2.1 Reaction Mechanism of HER

The electrochemical HER process follows two proton-coupled electron transfer mechanisms for HER. The HER mechanism (in the acidic medium) generally involves two reaction steps, which can be explained by Volmer-Heyrovsky or Volmer-Tafel mechanisms, as shown schematically in **Figure 3.3** The primary step is discharge step (Volmer reaction) in which a hydronium ion (H_3O^+) transfer from the solution to the surface of the catalyst and reacts with cathodic electron to provide H_{ads} (**equation 3.9**) [150]-

$$H_3O^+ + e^- \rightleftharpoons H_{ads} + H_2O \tag{3.9}$$

The Tafel's slope for Volmer reaction is known to be around 120 mV dec^{-1}. The Volmer step can then be followed by one of the two possible steps: (i) The Heyrovsky step (Tafel's slope ~40 mV dec^{-1}) in which a hydronium ion in solution combines with an adsorbed proton on the surface of the catalyst as followed by **equation 3.10** -

$$H_{ads} + H_3O^+ + e^- \rightleftharpoons H_2 + H_2O \tag{3.10}$$

(ii) Tafel step (Tafel's slope ~30 mV dec^{-1}) where two H_{ads} in the vicinity combine on the surface of the electrode to give a molecular hydrogen followed by **equation 3.11** -

$$H_{ads} + H_{ads} \rightleftharpoons H_2 \tag{3.11}$$

Theoretical and experimental studies in literature suggest that Pt has high surface coverage for adsorbed hydrogen ($\theta_H \approx 1$), so evolution proceeds by the Volmer-Tafel

mechanism, while H_{ads} coverage for MoS_2 is observed around $\theta_H \approx 0.25\text{-}0.5$, which favour the electrochemical desorption oriented Volmer-Heyrovsky mechanism [151,152].

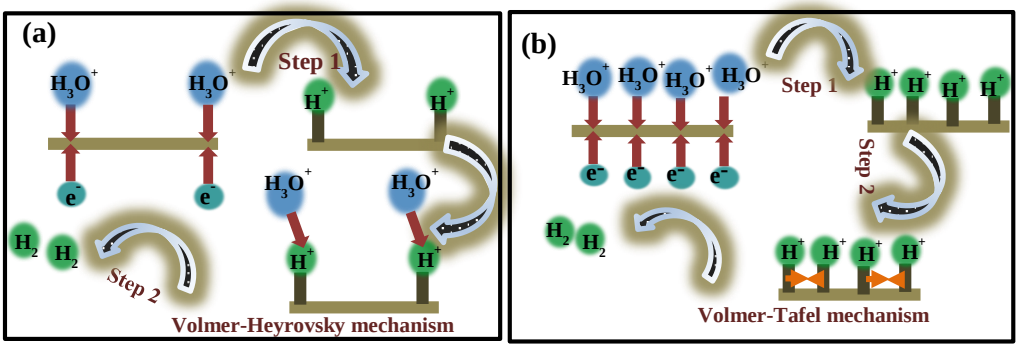

Figure 3.3 *Mechanisms for hydrogen evolution on the surface of an electrode in acidic media in Volmer-Heyrovsky (a)and Volmer-Tafel (b).*

3.2.2 Volcano Plot

The preceding explanation suggests that the adsorption and desorption of hydrogen on a catalyst surface follow two successive steps and according to the Sabatier principle, the interaction between catalysts surface and hydrogen atom should be appropriate. If the interaction is too weak hydrogen atom cannot efficiently adsorb on the surface of the catalyst, which will delay the HER process. On the other hand, if the interaction is too strong, catalyst would have difficulty to dissociate the hydrogen and clog the active sites, halting the completion of HER. Therefore, the catalyst should possess intermediate bonding energies with reactive intermediates to obtain optimal catalytic activity [153]. In 1958, Parson established a "volcano-type" plot and pointed out the optimal circumstances to attain the maximum exchange current density (j_o) at which value of Gibbs energy ($\mathbf{\Delta}G$) should be close to zero [1]. As shown in **Figure 3.4** the volcano peak is located at $\mathbf{\Delta}G=0$. The metals on the left-hand side of the volcano plot ($\mathbf{\Delta}G<0$) interact too strongly with the H^+ on the catalyst surface. The absorption of certain metals is quick, but the desorption is slow while the metals on the right of the graph ($\mathbf{\Delta}G >0$), have a weak affinity with the

proton, making interaction with active sites more difficult. The reaction continues quickly through the desorption process once the proton has been absorbed on the catalyst surface. Thus, the optimal electrocatalyst is the one which has a free energy of approximately zero and a high exchange current density value.

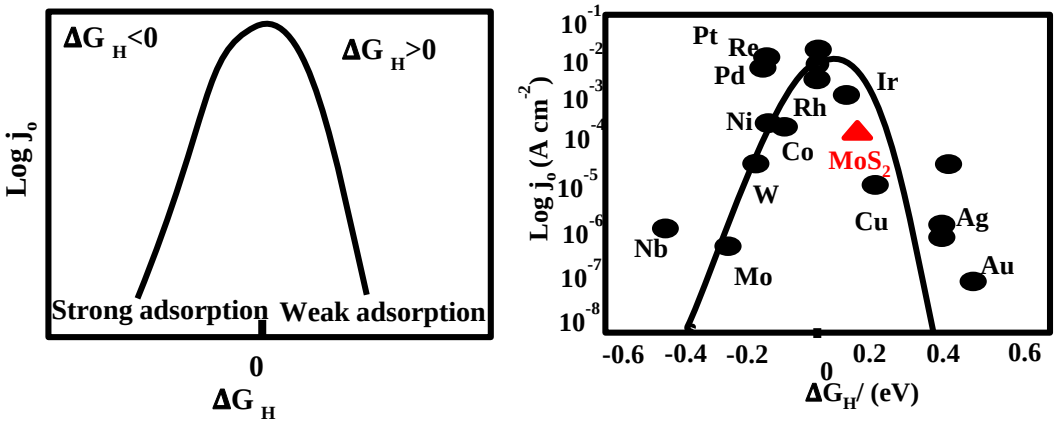

Figure 3.4 *(a) Valcano plot predicting catalysts with zero hydrogen binding energy will have the highest activity, (b) Volcano plot showing probable electrocatalysts for HER* [1].

The Pt sits at the top of volcano plot and has been proved to be the optimal catalyst with almost thermo-neutral ΔG_H. The scarcity and high cost of Pt limit its extensive technological application. An ideal catalyst for suitable HER should be made from inexpensive and readily available chemicals. The development of MoS_2 nanostructures, which present a high activity and acid stability, can significantly improve the HER [154]. The surface of bulk MoS_2 comprises of thermodynamically favourable basal plane sites, which are catalytically inert. In contrast, the edge sites of MoS_2 are catalytically active towards HER. In 2005, Hinnemann *et al.* performed a DFT simulation on Mo (1010) edge of MoS_2, indicating that at 50% hydrogen coverage, it has a **Δ**G of 0.08 eV, close to the ideal value [155]. Soon after, Jaramillo and co-worker experimentally confirmed that the edges of MoS_2, prepared by physical vapour deposition over Au substrate, are indeed catalytically active for the HER. The HER was found to be proportional to the length of the exposed edges rather than the coverage of MoS_2 nanoparticles, validating Hinnemann's

estimates [153]. Hence, the edge sites in MoS_2 nanostructures are regarded as preferable active sites for HER.

3.3 Results and Discussion

3.3.1 Reduced Graphite Oxides Electrodes for HER

In this section, we have discussed the HER study for hydrothermally synthesized rGO nanostructures-based electrodes. This section deals with the characterization and investigation of electrochemical activity of hydrothermally synthesized rGO-HH and rGO-Urea based electrodes. We have performed the linear sweep voltammetry (LSV) and electrochemical impedance spectroscopy (EIS) studies to investigate the HER activity of rGO samples.

3.3.1.1 Characterization of rGO Samples

Morphologies, structure and vibrational characteristics of rGO samples are confirmed by electron microscopy, diffraction and spectroscopy techniques. **Figure 3.5 (a)** and **(b)** show the SEM images for rGO-HH and rGO-Urea, respectively, depicting the presence of crumpled and overlapped sheets in rGO samples. **Figure 3.5 (c)** shows the XRD patterns for rGO-HH and rGO-Urea, providing the structural information. A peak for (002) plane along the c-axis is found at around 25° for both rGO samples. This peak position corresponds to the interlayer spacing around 0.35 nm due to the removal of intercalated oxygen atoms, indicating an efficient reduction of GO. Crystallite sizes along c-axis for rGO-HH and rGO-Urea are observed to be around 1.2 nm using Debye-Scherer formula, suggesting clusters of three to four graphene sheets in each stack of rGO samples [156,157]. **Figure 3.5 (d)** show the Lorentz function fitted Raman spectra for rGO-HH and rGO-Urea. It indicates the presence of a characteristic G-band along with the defect D-band in both the samples. The presence of D-band may be attributed to the presence of wrinkled

structure and oxygen-containing functional groups due to the chemical reduction. The G-band belongs to the in-plane vibrations of sp^2 hybridized carbon atoms. The D and G bands are observed at lower Raman shift values of ~1350 and 1585 cm^{-1}, respectively for rGO-HH compared to that for rGO-Urea (~1352 and 1589 cm^{-1}, respectively). The presence of a sharper G band for rGO-HH (FWHM~ 58 cm^{-1}) compared to rGO-Urea (FWHM~ 71 cm^{-1}) may suggest the uniform distribution of long range order of sp^2 network in rGO-HH compared to rGO-Urea [158,159]. The peak ratios for D and G bands, i.e. I_D/I_G is found to be around 0.89 and 0.98 for rGO-HH and rGO-Urea, respectively, indicating the presence of lesser defects in rGO-HH.

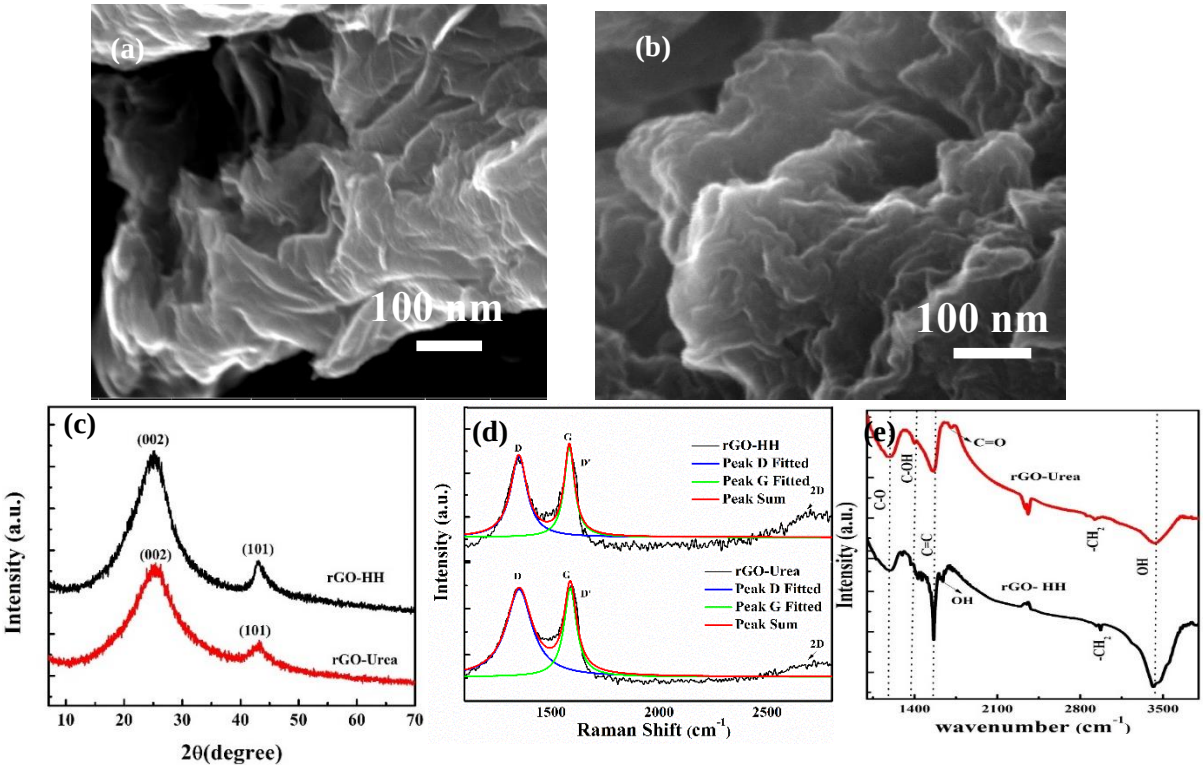

Figure 3.5 *SEM images of (a) rGO-HH and (b) rGO-Urea, (c) XRD patterns, (d) Raman spectra and (e) FTIR spectra for rGO-HH and rGO-Urea.*

Figure 3.5 (e) indicates the FTIR spectra for both rGO samples, suggesting the presence of different functional groups such as hydroxyl, carboxylic, carbonyl etc. The rGO samples show the presence of C-O (~ 1190 cm^{-1}), C-OH (~ 1384 cm^{-1}) and -OH (~ 1682 cm^{-1}) vibrational modes along with characteristic peak for in-plane vibrations of C=C. The

presence of a sharper and stronger C=C (~ 1550 cm^{-1}) peak in rGO-HH clearly indicates the longer-range order of sp^2 network in rGO-HH compared to that for rGO-Urea [97], [160]. The absence of C=O in rGO-HH suggest the better removal of epoxide via hydrazine reduction route, which may lead to better electrical conduction in rGO-HH compared to that in rGO-Urea.

3.3.1.2 Electrochemical Activity of rGO Electrodes

As per literature report, the rGO nanostructures do not show good catalytic activity. We have investigated the catalytic activity of as synthesized rGO-HH and rGO-Urea nanosheets for HER in the acidic electrolyte (0.5 M H_2SO_4) using a conventional three cell setup. **Figure 3.6 (a) and (d)** demonstrates the LSV measurements for rGO-HH and rGO-Urea electrodes at scan rates of 5 and 10 mV s^{-1}. Absence of any vigorous increment in the current density suggests poor catalytic activity of both rGO samples towards HER. As the HER mechanism of an electrocatalyst is decided based on the Tafel slope, the polarization curves are fitted using Tafel's **equation 3.8**. The Tafel slopes of the rGO-HH and rGO-Urea have been accordingly calculated at different scan rates to analyse the HER kinetics as shown in **Figure 3.6 (b, e)**. The value of Tafel's slope value of ~ 411 and 904 mV per dec^{-1} have been obtained at a voltage sweep rate of 5 mV s^{-1} for rGO-HH and rGO-Urea, respectively, implying the poor catalytic activity due to the absence of any active sites in rGOs samples.

To further investigate the electrode kinetics and charge transfer at electrode/electrolyte interface, EIS measurement has been performed for both rGO samples. **Figure 3.6. (c) and (f)** show the Nyquist plots of the rGO-HH and rGO-Urea, respectively, fitted using constant phase element (CPE) equivalent circuits due to the dispersive nature of Nyquist plots [161]. The EIS data is fitted using Zsimpwin software.

The rGO-HH and rGO-Urea shows uncompensated solution resistance R_s~ 2.3 and 1.06 Ω and charge transfer resistance R_{ct} ~57 and 294 Ω, respectively. The higher value of charge transfer suggests poor catalytic activity of rGO samples towards HER. In summary, we observed that the prepared rGO samples show poor electrocatalytic activity for HER study. The rGO-HH possess larger and uniform dimensions, which can provide more stable electrochemical behaviour compared to rGO-Urea. However, the lack of metal active sites in rGO samples limits their use as electrocatalysts for HER.

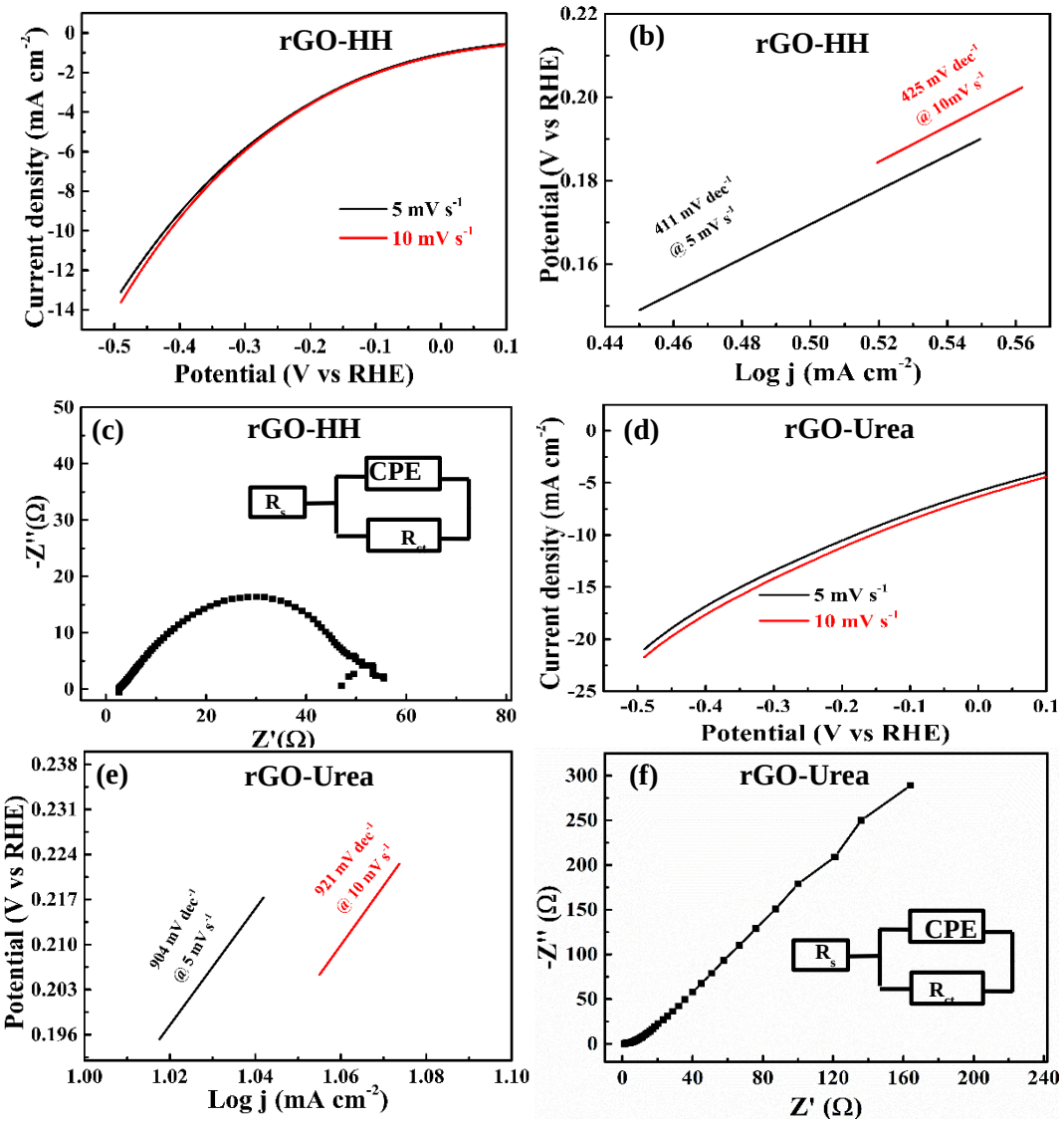

Figure 3.6 *(a) LSV curves, (b) Tafel plots, and (c) Nyquist plot for rGO-HH electrodes, (d) LSV curves, (e) Tafel plots, and (f) Nyquist plot for rGO-Urea electrodes.*

3.3.2 MoS_2 Nanoclusters Electrodes for HER

During the synthesis of MoS_2 nanostructures, thioacetamide reacts with water at high temperature and releases H_2S gas, which acts as a sulphur source as well as reducing agent to reduce the sodium molybdate to yield desired MoS_2 nanostructure. The expected reaction route for synthesis of MoS_2 nanostructures is illustrated in following **equations (3.12-3.13)** [117], [118]-

$$\boldsymbol{2CH_3CSNH_2 + 4H_2O \rightleftharpoons 2CH_3COOH + 2NH_3 + 2H_2S} \quad (3.12)$$

$$\boldsymbol{4MoO_4^{2-} + 9H_2S + 6CH_3COOH \rightleftharpoons 4MoS_2 + SO_4^{2-} + 6CH_3COO^- + 12H_2O} \quad (3.13)$$

In the present work, we have obtained different morphologies of MoS_2 nanostructures (nanoclusters, nanoflowers and nanosheets) by varying the reaction time in hydrothermal process and by use of additional reducing agent. This section deals with the characterization and investigation of HER activity of 2H-MoS_2 nanoclusters, synthesized via hydrothermal process for 24 h. To investigate the electrochemical activity and stability of MoS_2 nanoclusters-based electrodes for HER, we have performed LSV and EIS studies.

3.3.2.1 Characterization of MoS_2 Nanoclusters

The morphological study of MoS_2 nanoclusters is performed using SEM. **Figure 3.7 (a)** shows the SEM image for synthesized MoS_2, demonstrating the uniform distribution of large quantities of well-separated nanoclusters. These nanoclusters are composed of multiple agglomerated sheets of MoS_2, as marked in the SEM image. The lateral dimensions of the nanoclusters are found in the range of 300-500 nm. **Figure 3.7 (b)** shows XRD pattern of MoS_2 nanoclusters indicating the characteristic peaks of MoS_2 at 14.2°, 32.7°, 35.5°, 43.6° and 57.7°, corresponding to the (002), (100), (103), (105) and (110) planes, respectively. The intense peak located at 14.2° validates the formation of hexagonal

phase 2H-MoS_2 (JCPDS card no.37-1492). The Scherrer calculation using broadening of (002) plane provides the information about the thickness of each cluster [162], which is found to be around 6 nm with inter layer spacing of 0.63 nm. This indicates the average number of layers to be around 10 in each nanocluster. The vibrational characteristics of synthesized MoS_2 nanoclusters have been examined using Raman and FTIR spectroscopy techniques. The observation of two Raman peaks at 377 and 403 cm^{-1} confirms the formation of 2H phase in MoS_2 nanoclusters, as shown in **Figure 3.7 (c)**. The peak at 377 cm^{-1} represents the E^1_{2g} (in-plane motion of Mo and S) vibrational mode, while peak at 403 cm^{-1} represents the A_{1g} (out of plane motion of S) mode [163]. The out of plane motion of 2H phase MoS_2 nanoclusters (A_{1g} mode) suggests stacking of few layers in each nanocluster as observed in the form of (002) plane of the XRD pattern. The peak separation between E^1_{2g} and A_{1g} modes is estimated at around 26 cm^{-1}, propounding the presence of multiple layers in each cluster of MoS_2 [164,165]. Absence of any other Raman peaks clearly suggests the purity of 2H phase in synthesized MoS_2 nanoclusters. The FTIR spectrum of MoS_2 nanoclusters is given in **Figure 3.7 (d)**, which indicates the presence of multiple broad and sharp absorption bands. The weak band of Mo=O at 908 cm^{-1} is observed due to the presence of moisture [166]. The peak observed at 1189 and 1620 cm^{-1} attribute the presence of carboxylic (-COOH) and carbonyl (C=O) groups. The weak peak at 466 cm^{-1} is attributed to the Mo-S vibrations and the strong peak at 3402 cm^{-1} belongs to the characteristic stretching vibration of the hydroxyl (-OH) group. The availability of these functional groups provides good wettability to MoS_2 nanoclusters, which improves the better utilization of active sites and hence better HER activity.

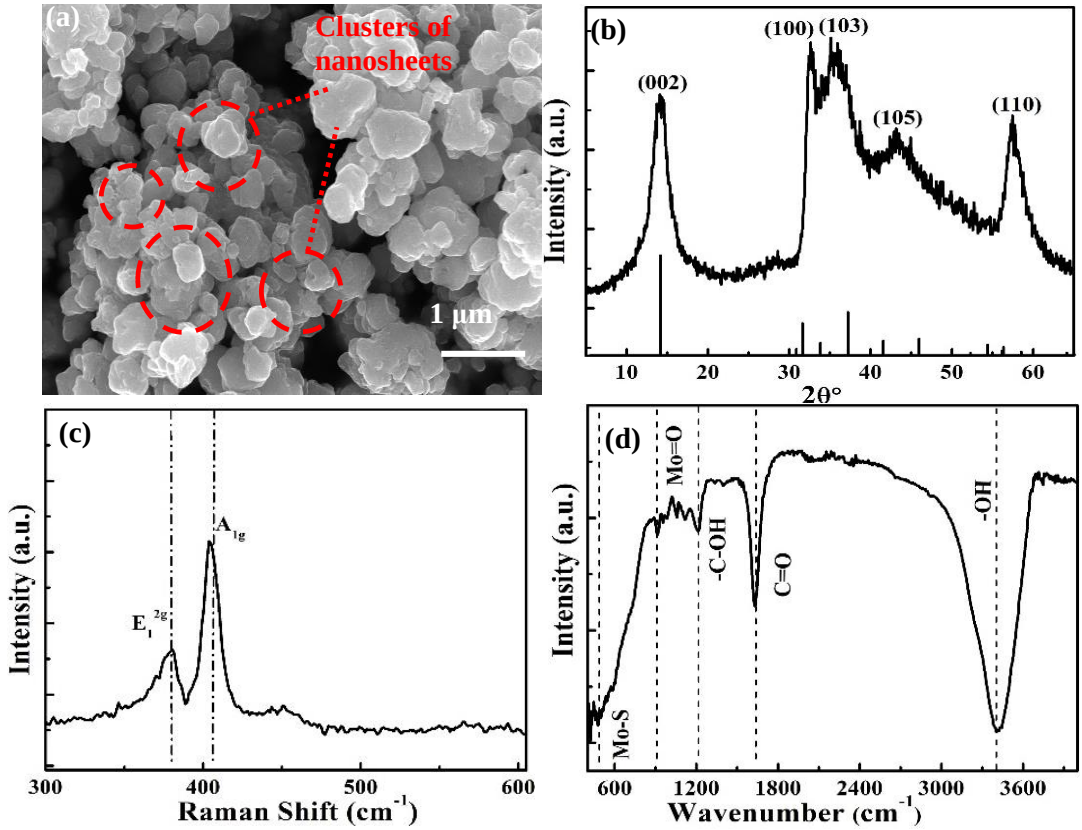

Figure 3.7 *(a) SEM image, (b) XRD pattern, (c) Raman spectrum and (d) FTIR spectrum for MoS_2 nanoclusters.*

3.3.2.2 Electrochemical activity of MoS_2 nanoclusters Electrodes

To understand the catalytic activity of MoS_2 nanoclusters coated conducting carbon paper electrode for HER, LSV and EIS measurements have been performed. The LSV curves of MoS_2 nanoclusters electrode and bare conducting carbon paper are shown in **Figure 3.8 (a)**. As expected, MoS_2 nanoclusters displayed enhanced catalytic activity with low onset potential of 0.132 V. The Tafel slopes for MoS_2 nanoclusters at different scan rates are plotted in **Figure 3.8 (b)**. The values of Tafel slope of MoS_2 nanoclusters electrode are found to be 103, 123, 211 and 321 mV dec^{-1} at different scan rates of 2, 5, 10 and 20 mV s^{-1}, respectively. The LSV curve for 2H phase MoS_2 nanoclusters at 2 mV s^{-1} indicates onset potential (0.132V) along with over-potential (η_{10}) around 0.212 V with respect to RHE at a current density of 10 mA cm^{-2}. These results indicate that the synthesized MoS_2 nanoclusters follow two proton-coupled electron transfer mechanism for HER. The

observed value of the Tafel slope is103 mV dec^{-1} for MoS_2 nanoclusters in the present work suggests that the Volmer step is the rate-determining step which is followed by the desorption step. Hence, the HER activity of MoS_2 nanoclusters is expected to follow the Volmer-Heyrovsky mechanism. The catalytic activity of MoS_2 nanocluster decreases at a higher scan rate due to the decrease in accessible active sites and lesser time for H^+ ions for adsorption/desorption. The interfacial reactions and electrode kinetics of MoS_2 nanoclusters in HER are further examined by EIS measurement. **Figure 3.8 (c)** shows Nyquist diagram of MoS_2 nanoclusters is fitted using CPE equivalent circuit as shown in inset. The presence of a semicircle in the Nyquist plot indicates the charge transfer process at electrode/electrolyte interface, which is associated with charge transfer resistance (R_{ct}). In addition to R_{ct} such process also contains uncompensated solution resistance R_s as shown in inset of **Figure 3.8 (c)** [161]. The Nyquist plot of MoS_2 nanoclusters shows uncompensated solution resistance R_s∼1.52 **Ω** and low charge transfer resistance R_{ct}∼83 **Ω**, which reflect significant electron transfer rate for HER and hence significant electrocatalytic activity of prepared 2H phase MoS_2 nanoclusters [167,168]. Further, the stability of MoS_2 nanoclusters electrode has been examined to identify its robustness in acidic medium. The stable current density is observed for 2000 cycles at scan rate of 20 mV sec^{-1}, as shown in the inset of **Figure 3.8 (d)**. It clearly suggests the quite stable nature of MoS_2 nanoclusters electrode in acidic medium for HER study.

In summary, the electrochemical study of prepared 2H phase MoS_2 nanoclusters suggests significantly low values of Tafel slope and overpotential, which makes it a reasonable electrode material for HER study. The significant catalytic activity can be attributed to available active sites of MoS_2 nanoclusters and improved wettability due to oxygen-containing functional groups.

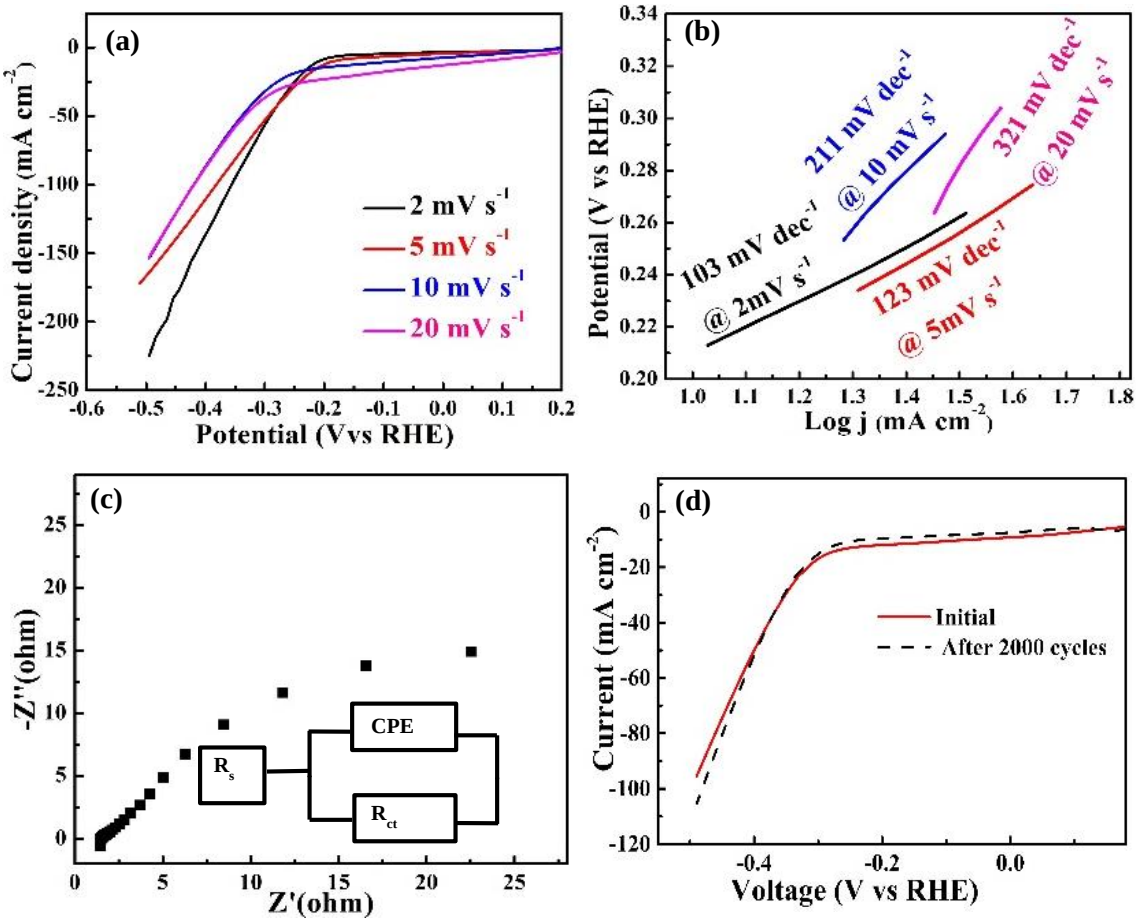

Figure 3.8 *(a) LSV curves at different voltage scan rates, (b) Corresponding Tafel plots, (c) Nyquist Plot of MoS_2 nanoclusters and (d) stability test for MoS_2 nanoclusters electrode at 20 mV s^{-1}.*

3.3.3 MoS_2 Nanoflowers Electrodes for HER

This section deals with the characterization and investigation of electrochemical activity of 2H phase MoS_2 nanoflowers, synthesized in 48 h of hydrothermal process. The LSV, EIS and stability measurements have been performed to observe the catalytic activity of MoS_2 nanoflowers-based electrodes for HER.

3.3.3.1 Characterization of MoS_2 Nanoflowers

The morphological study of as-prepared flower like MoS_2 nanostructure was performed with electron microscopy techniques. The SEM image of synthesized MoS_2 shows the presence of uniform 3D flower-like nanostructures, as shown in **Figure 3.9 (a)**. The TEM image further confirms the 3D flower like structure of prepared MoS_2. Different

well separated nanoflakes of MoS_2 are wrapped as petals in ordered manner resulting in flower like structure with exposed edges as shown in **Figure 3.9 (b)**. The flower-like nanostructures have outer diameters in the range 200-300 nm. **Figure 3.9 (c)** shows high-resolution TEM image, depicting the presence of 7 to 10 layers with interplanar spacing of around 0.64 nm in different wrapped petals. **Figure 3.9 (c)** also indicates discontinuity in petals suggesting the presence of defects in synthesized MoS_2 nanoflowers [169]. **Figure 3.9 (d)** shows XRD pattern of MoS_2 nanoflowers, indicating the characteristic peaks at 14.3°, 33.6°, 39.7° and 59.0°, corresponding to the (002), (100), (103) and (110) plane, respectively. A sharp peak at 14.3° confirms the well-defined and hexagonally symmetric crystalline structure (JCPDS card no.37-1492). The Scherrer analysis using (002) diffraction plane indicates the presence of 8 to 10 layers of MoS_2 in each petal of MoS_2 nanoflowers [170,171]. Further phase and purity of sample is confirmed using Raman study, as shown in **Figure 3.9 (e)**. The presence of two prominent characteristic Raman peaks at 378 cm^{-1} (E^1_{2g} mode) and 403 cm^{-1} (A_{1g} mode) confirms the formation of hexagonally symmetric 2H phase of MoS_2 nanoflowers. The separation between E^1_{2g} and A_{1g}modes is found around 25 cm^{-1}, suggesting the presence of more than 6 layers in petals of MoS_2 nanoflowers [171,172]. The less intense broad peak at 455 cm^{-1} appears in few layer MoS_2 due to the second order process having longitudinal acoustic phonon at M points [173]. FTIR spectrum of MoS_2 nanoflowers is shown in **Figure 3.9 (f)**, which indicates the presence of broad absorption bands. The peaks observed at 908, 1040, 1197 and 1620 cm^{-1} attribute to the presence of S-S, C-O, -C-OH and C=O bonds, respectively [174,175]. A weak peak is observed at 466 cm^{-1}, which attributes to the Mo-S vibrations and the broad band at 3000-3500 cm^{-1} belongs to the characteristic stretching vibration of the hydroxyl (OH) group [176]. The presence of oxygen containing functional groups

enhances the wettability of prepared MoS_2 and facilitates the electrolyte transport to improve the electrochemical activity of MoS_2 nanoflowers.

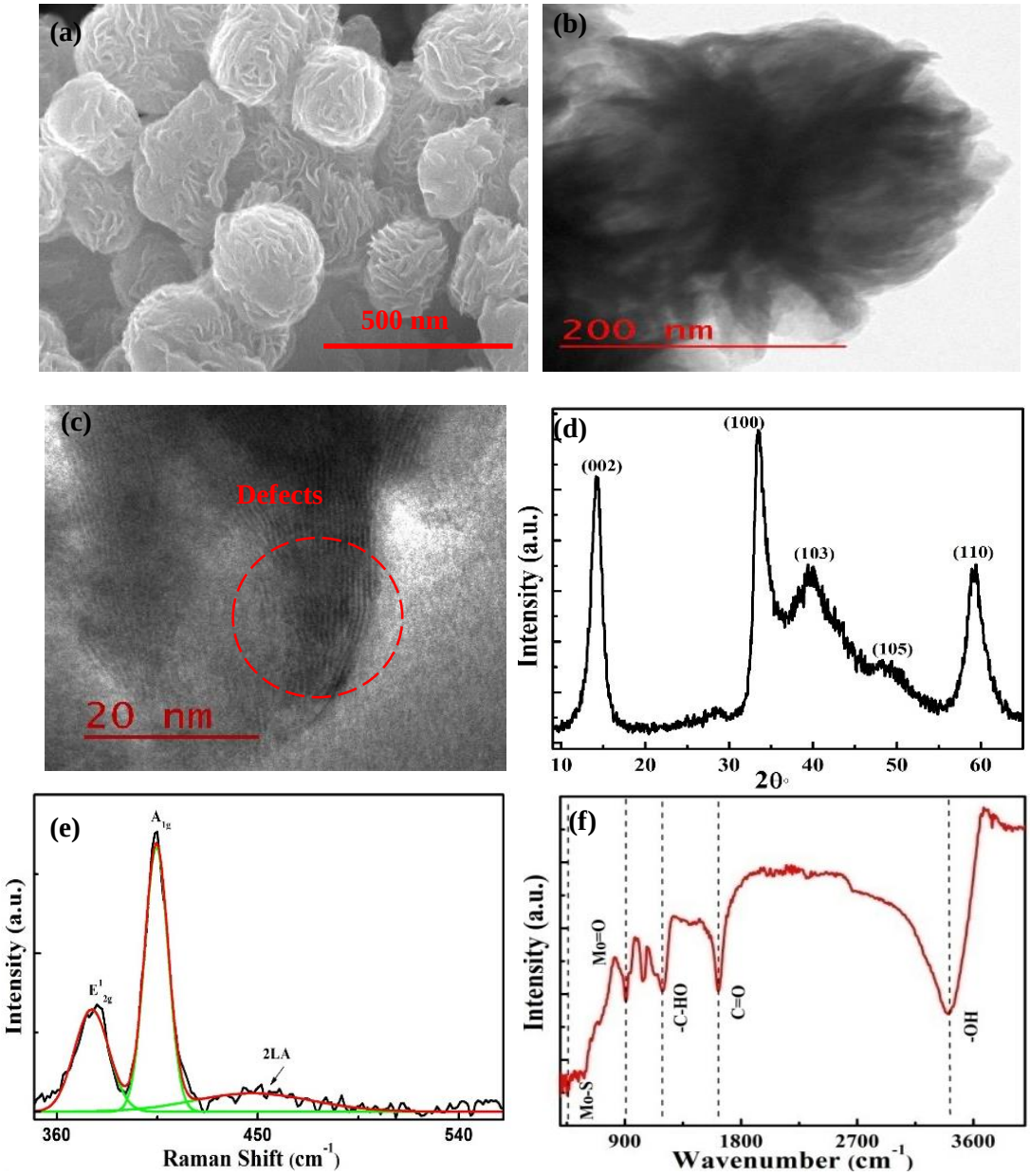

Figure 3.9 *(a) SEM, (b) TEM, (c) HRTEM images, (d) XRD pattern, (e) Raman spectrum, and (f) FTIR-spectrum for MoS_2 nanoflowers.*

3.3.3.2 Electrochemical Activity of MoS_2 Nanoflowers Electrodes

The electrocatalytic HER activity of the as-prepared 2H-MoS_2 nanoflowers catalysts has been evaluated in acidic (0.5 M H_2SO_4) medium with a typical three-electrode configuration. The LSV curves of as prepared MoS_2 nanoflowers coated carbon paper

electrode at different voltage scan rates are shown in **Figure 3.10 (a)**. As anticipated, the MoS_2 nanoflowers show excellent catalytic activity due to the presence of defects and a large number of exposed edges in well separated petals. Generally, the intrinsic activity of HER catalyst is represented in terms of Tafel slope, smaller the Tafel slope better the HER activity. The Tafel slopes of the catalyst at different scan rates are shown in **Figure 3.10 (b)**. The Tafel slope value of MoS_2 nanoflowers is found to be around 69, 122 and 167 mV dec^{-1} at scan rate of 5, 10 and 20 mV s^{-1}, respectively suggesting the excellent hydrogen evolution activity of synthesized MoS_2 nanoflowers. The onset potential and the overpotential of HER activity of MoS_2 nanoflowers are 122 and 193 mV, respectively. The low values of Tafel slope and overpotential for MoS_2 nanoflowers suggest its better HER activity and faster kinetics, which may be associated with higher number of active sites due to the presence of defects and exposed edges in flower like structures. **Figure 3.10 (c)** shows Nyquist plot of MoS_2 nanoflowers in frequency range of 0.01 to 10^5 Hz in 0.5 M H_2SO_4 electrolyte at overpotential fitted using constant phase element (CPE) equivalent circuit, shown as inset [177]. The small values of R_S~ 1.48 Ω and R_{CT}~ 51 Ω are observed, which suggests the faster faradic process and better HER kinetics of prepared MoS_2 nanoflowers. The HER activity for MoS_2 nanoflowers is found to follow two step Volmer-Heyrovsky mechanism. The long-term acid stability of the as-prepared MoS_2 nanoflowers electrode has been investigated by demonstrating 2500 cycles of LSV at a constant scan rate of 20 mV s^{-1}. **Figure 3.10 (d)** shows negligible loss in current density after 2500 cycles suggesting the high degree of cyclic stability of MoS_2 nanoflowers electrodes for HER.

In summary, the electrochemical study comprising LSV, stability test and EIS measurements verify that the prepared 2H phase MoS_2 nanoflowers show low values of Tafel slope and overpotential, which makes it a promising candidate for HER. The excellent catalytic activity can be attributed to presence of exposed edges and active sites in MoS_2

nanoflowers. The stability and scalability of prepared MoS_2 nanoflowers make it a potent catalyst for hydrogen production at commercial scale.

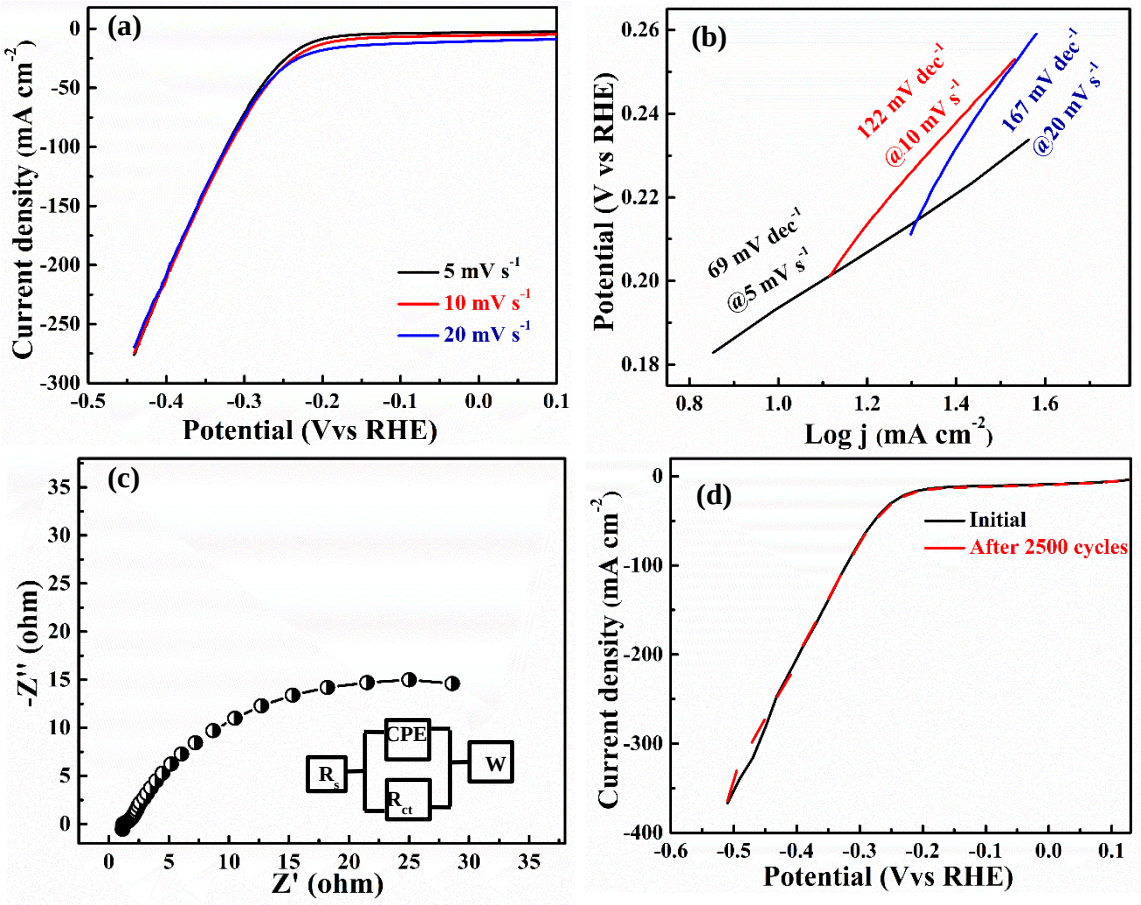

Figure 3.10 *(a) LSV curves at different scan rates, (b) Corresponding Tafel plots, (c) Nyquist plot and, (d) stability test at 20 mV s^{-1} for MoS_2 nanoflowers electrodes.*

3.3.4 MoS_2 Nanosheets Electrodes for HER

We have also studied the HER activity of hydrothermally synthesized MoS_2 nanosheets, prepared with use of additional use of hydrazine hydrate as a reducing agent. This section deals with the characterization and investigation of the electrochemical activity of hydrothermally synthesized MoS_2 nanosheets.

3.3.4.1 Characterization of MoS_2 Nanosheets

The morphology of as-synthesized MoS_2 nanosheets is investigated using SEM. **Figure 3.11 (a)** shows SEM image of synthesized MoS_2 nanosheets, indicating uniform

distribution of ultrathin nanosheets. The wrinkled nature and large number of edges in these ultrathin MoS_2 nanosheets may provide a large surface area and facilitate rapid electron transport during the electrochemical process. TEM study has been performed to observe the structure and the number of layers in each stack of MoS_2 nanosheets. **Figure 3.11 (b)** clearly suggests the formation of interconnected stacks of wrinkled nanosheets. The contrast between the wrinkled sheets has confirmed the formation of a few-layer structure with a large number of defects which facilitates high active surface area and a short diffusion path for electrolyte ions hence improves electrochemical performance [178]. HRTEM image of **Figure 3.11 (c)** indicates the curved edges of wrinkled nanosheets, suggesting the presence of defects and active sites with d-spacing~ 0.64 nm. Each stack of differently oriented nanosheets shows thickness in the range of 5-7 nm, indicating the presence of 7-10 layers in prepared MoS_2 nanosheets. Further, the crystallinity of MoS_2 nanosheets is validated using the XRD measurement. **Figure 3.11 (d)** shows the XRD pattern of MoS_2 nanosheets with standard peaks at 14.1°, 33.0° and 57.0°, which corresponds to (002), (100), and (110) plane, respectively. A broader peak at 14.1° of (002) plane confirms the formation well-stacked layered hexagonal (2H) crystal structure of MoS_2 (JCPDS card no.37-1492) [170]. The presence of no other peak in XRD pattern confirms high purity of as-synthesized MoS_2 nanosheets. The phase, crystallinity, and associated defect levels in synthesized MoS_2 nanosheets have also been confirmed by the Raman study. The MoS_2 nanosheets demonstrate two prominent characteristic peaks at 378 (E^1_{2g}) and 403 (A_{1g}) cm^{-1} in the Raman spectrum as shown in **Figure 3.11 (e)**, confirming the presence of hexagonal phase of as-synthesized MoS_2 [179]. The peak separation between E^1_{2g} and A_{1g} modes is found to be 27 cm^{-1}, suggesting that individual MoS_2 nanosheets have more than 8 layers which matches to our TEM analysis [180].

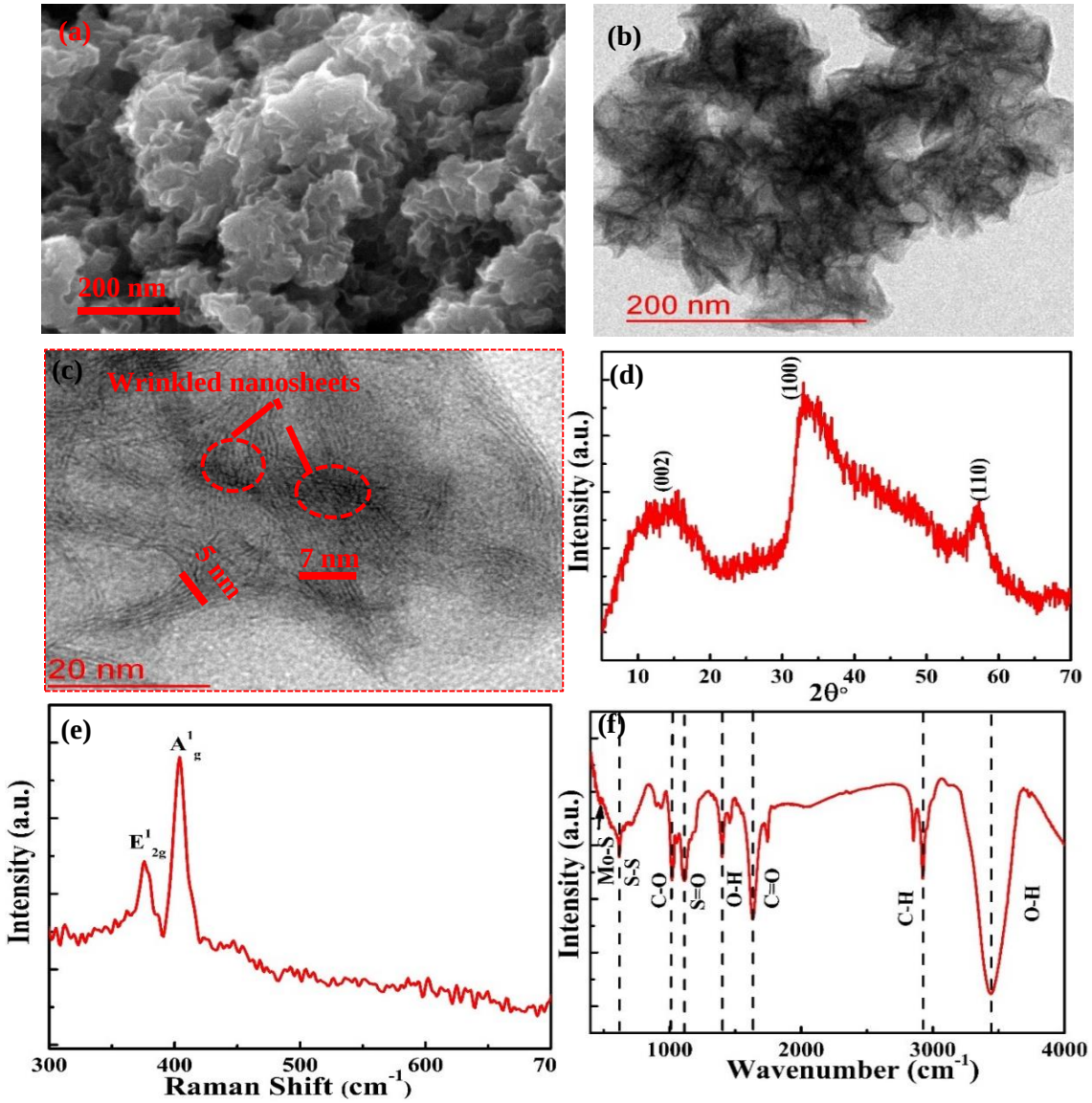

Figure 3.11 *(a) SEM, (b) TEM, (c) HRTEM images, (d) XRD pattern, (e) Raman spectrum, and (f) FTIR spectrum for MoS_2 nanosheets.*

Further, FTIR study has been performed to examine the functionality present in the synthesized 2H-MoS_2 nanosheets. **Figure 3.11 (f)** shows the FTIR spectrum of a MoS_2 nanosheets, revealing the existence of several absorption bands. The band at 476 and 620 cm^{-1} correspond to Mo-S and S-S bond vibrations of MoS_2 nanosheets, respectively [174], [181]. Further, presence of the absorption bands at 1024 and 1119 cm^{-1} are characteristic peaks of C-O and S=O stretching vibration, respectively [182,183]. The broad band at 1407 cm^{-1} is due to the O-H bending vibration, while the peaks appeared at 1643 cm^{-1} is possibly due to the presence of carbonyl group (C=O) [183]. The peak observed at 2922

cm^{-1} is attributed to the C-H asymmetric vibration and the peak at 3402 cm^{-1} belongs to the hydroxyl stretching vibrations [184]. The inclusion of oxygen containing functional groups enhances the electrode wettability and may facilitate the electrochemical activity of 2H-MoS_2 nanosheets.

3.3.4.2 Electrochemical Activity of MoS_2 Nanosheets Electrodes

The HER activities of the as-synthesized 2H-MoS_2 nanosheets electrodes have been investigated in acidic electrolyte (0.5 M H_2SO_4) using a conventional three cell setup. **Figure 3.12 (a)** demonstrates the LSV measurement of MoS_2 nanosheets electrode at varied scan rates. As expected, the 2H-MoS_2 nanosheets possess excellent catalytic activity due to large number of accessible edges in sheet like structure. The Tafel slopes of the catalyst have been accordingly calculated at different scan rates to analyse the HER kinetics, as shown in **Figure 3.12 (b)**. Tafel slopes of 83, 115, 186 and 287 mV s^{-1} are obtained at voltage sweep rate of 2, 5, 10 and 20 mV s^{-1}. The lowest value of Tafel's slope for 2H-MoS_2 nanosheets is found to be 83 mV dec^{-1} at voltage sweep rate of 2 mV s^{-1} with overpotential (η_{10}) ~ 206 mV, implying the good hydrogen evolution capability of MoS_2 nanosheets electrode. The low values of Tafel slope and over potential imply faster kinetics for HER activity. The catalytic activity of MoS_2 nanosheets decreases at higher scan rate due to the decrease in accessible active sites. The lower slope value shows that the creation of H_2 molecules over the catalyst surface occurs via the Volmer-Heyrovsky process in which the rate-limiting step is the interaction of H atom with proton to produce H_2 molecule [185].

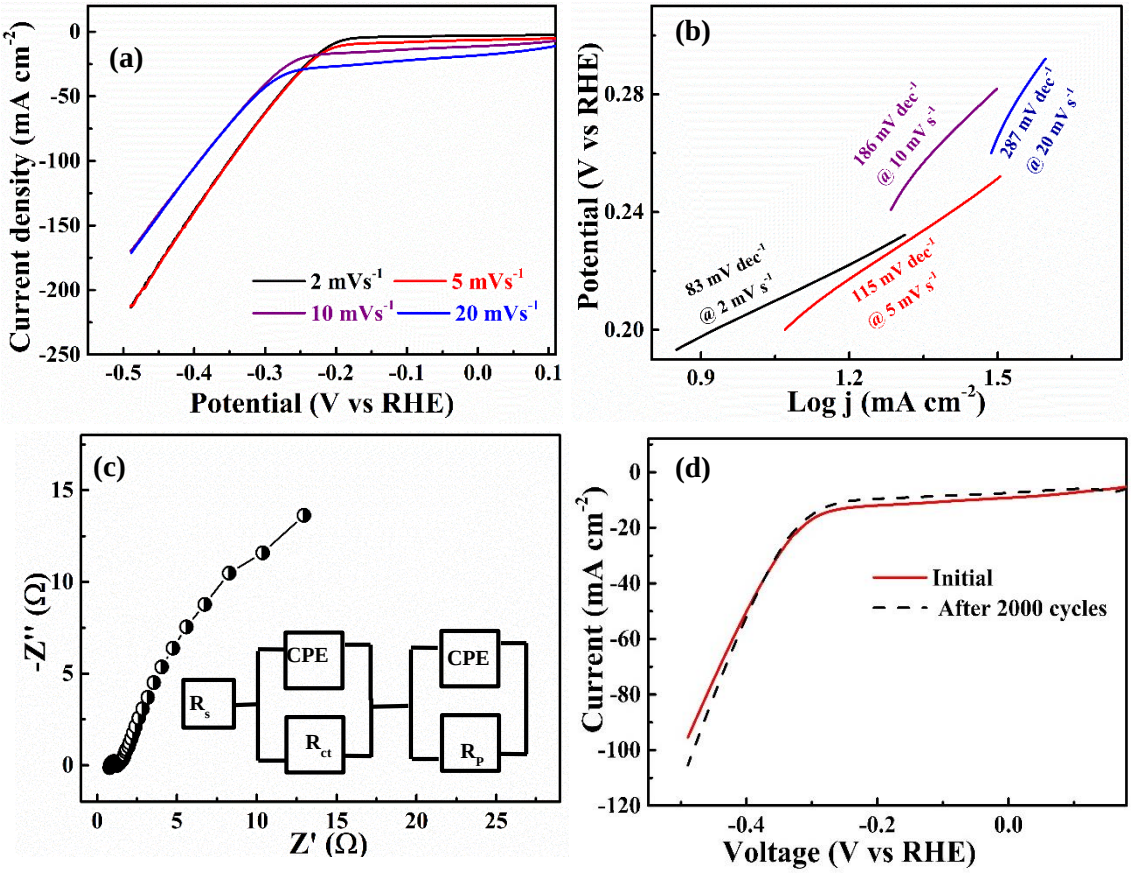

Figure 3.12 *(a) LSV curves at different scan rates, (b) Corresponding Tafel plots, (c) Nyquist plot, and (d) HER stability test at 20 mV s^{-1} for MoS_2 nanosheets electrode.*

EIS measurements have been used to investigate the interfacial reactions and electrode kinetics of 2H-MoS_2 nanosheets in the HER investigation. **Figure 3.12 (c)** shows the Nyquist plot of MoS_2 nanosheets electrodes, indicating low value of R_s~ 0.6 Ω and R_{ct} ~1.42 Ω, implying the faster faradic process and hence superior HER performances of synthesized MoS_2 nanosheets. **Figure 3.12 (d)** shows the stability curve of as-synthesized MoS_2 nanosheets electrode for HER, exhibiting 2000 cycles of LSV at sweep rate of 20 mV s^{-1}. There is negligible loss in current density after 2000 cycles, indicating higher degree of cyclic stability of 2H-MoS_2 nanosheets for hydrogen evolution. The long-term durability of synthesized MoS_2 nanosheets for HER can be considered as an important parameter for its commercial viability. In summary, the smaller values of Tafel's slope, overpotential and resistances for MoS_2 nanosheets depicts its improved HER activity due to the presence of active sites associated with large number of edges in sheet like structure.

3.3.5 MoS_2-rGO Heterostructure Electrodes for HER

After examining the HER activity of different rGO and MoS_2 nanostructures, we observe that rGO is poor electrocatalyst while MoS_2 nanoflowers and nanosheets shows good catalytic response for HER. Although rGO does not show catalytic behaviour but it is known as good conducting material with high surface area and it is used in different electrochemical applications. In order to utilize the synergistic effect between rGO and MoS_2 nanosheets, we have synthesized MoS_2-rGO heterostructure using rGO along with Mo and S precursors and hydrazine hydrate as reducing agent in hydrothermal process and investigated the catalytic activity of heterostructure. This section deals with the characterization MoS_2-rGO heterostructure and investigation of electrochemical activity of MoS_2-rGO heterostructure coated carbon paper electrodes. To investigate the HER activity LSV, stability and EIS measurements have been performed for MoS_2-rGO heterostructure electrodes.

3.3.5.1 Characterization of MoS_2-rGO Heterostructure

The SEM analysis provides the information about the morphology of as-synthesized MoS_2-rGO heterostructures, as shown in **Figure 3.13 (a)**. It shows that crumpled and wrinkled MoS_2 nanosheets are well distributed on the rGO sheets of larger dimensions. The TEM study is further used to analyze the structure of as-prepared MoS_2-rGO heterostructure, as shown in **Figure 3.13 (b)**, which clearly confirm the observation of SEM image that self-assembled sheet-like MoS_2 nanostructures are loaded on skeleton of rGO sheets. **Figure 3.13 (c)** shows the XRD pattern of as synthesized MoS_2-rGO heterostructure, exhibiting clear diffraction peaks of MoS_2 at 14.3°, 33.6°, 39.7° and 59.0°, corresponding to the (002), (100), (103) and (110) plane, respectively, along with a small hump around 25°, which corresponds to (002) plane of graphitic structure along c-axis and confirms the presence of rGO nanosheets in heterostructures.

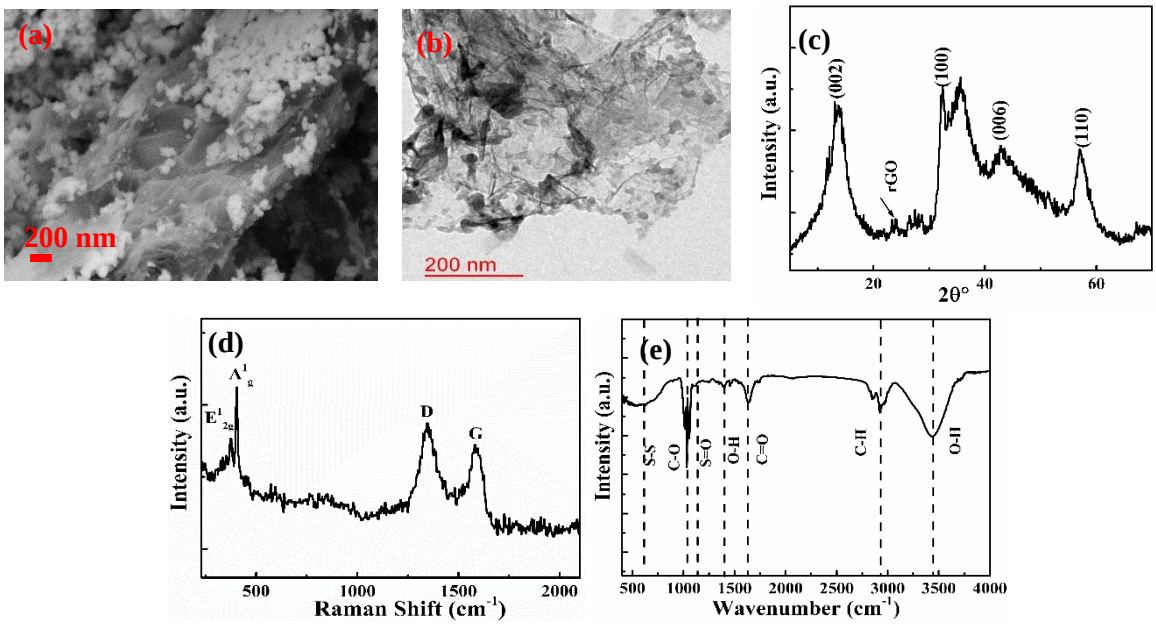

Figure 3.13 *(a) SEM, (b) TEM images, (c) XRD pattern, (d) Raman spectrum, and (e) FTIR spectrum for MoS_2-rGO* heterostructure.

Figure 3.13 (d) shows Raman spectrum of MoS_2-rGO heterostructure comprising the characteristic bands for MoS_2 and rGO, which confirms the formation of heterostructure. Raman peaks at 378 cm^{-1} (E^1_{2g} mode) and 403 cm^{-1} (A_{1g} mode) confirm the formation of 2H phase of MoS_2 along with the peak at 1355 and 1598 cm^{-1} corresponding to the D- and G-bands, respectively, for rGO in heterostructure. **Figure 3.13 (e)** shows FTIR-spectrum of MoS_2-rGO heterostructure, indicating the presence of broad absorption bands. The broad band at 908 cm^{-1} is observed due to the S-S bond. The presence of different oxygen-containing functional groups at 1040, 1197 and 1620 cm^{-1} are attributed to C-O, -C-OH and carbonyl group (C=O), respectively. The weak peak is observed at 466 cm^{-1} attributes to Mo-S vibrations and the broadband at 3000-3500 cm^{-1} belongs to the characteristic stretching vibration of the hydroxyl (OH) group. These oxygen-containing functional groups enhance the wettability of as prepared MoS_2-rGO heterostructure and facilitates the electrolyte transport to improve the electrochemical activity.

3.3.5.2 Electrochemical Activity of MoS_2-rGO Heterostructure Electrodes

To further understand electrocatalytic HER activity of as-prepared MoS_2-rGO heterostructure electrodes, we have performed the electrochemical study in an acidic (0.5 M H_2SO_4) medium with a typical three-electrode configuration. The catalytic activity of heterostructure electrodes have been obtained by performing LSV study at different voltage sweep rate, as shown in **Figure 3.14 (a)**. The Tafel plots of the catalyst are accordingly calculated to examine the HER kinetics as shown in **Figure 3.14 (b)**. The smallest Tafel slope value~ 90 mV dec^{-1} and overpotential~ 194 mV are found at a scan rate of 2 mV s^{-1}, suggesting the good hydrogen evolution activity of as synthesized MoS_2-rGO heterostructure. The MoS_2-rGO heterostructure shows good catalytic activity due to the presence of defects and active sites of in-situ synthesized heterostructure. **Figure 3.14 (c)** shows Nyquist plot of MoS_2-rGO heterostructure in frequency range of 0.01 to 10^5 Hz in 0.5 M H_2SO_4 electrolyte at overpotential and fitted using CPE equivalent circuit shown as inset [177]. The fitted circuit shows the small value of R_s~ 1.17 Ω along with R_{ct} ~2.4 Ω for as prepared MoS_2-rGO heterostructure, which suggests the faster faradic process and better HER kinetics. The lower values of Tafel slope, resistances and overpotential suggests that HER follows Volmer-Heyrovsky mechanism and its better HER activity is associated with presence of defects, availability of functional groups and edges in the heterostructure. The acid stability of as-prepared MoS_2-rGO heterostructure electrode is investigated by demonstrating 1500 cycles of LSV at a constant scan rate of 20 mV s^{-1}, which suggests negligible loss in current density after 1500 cycles, as shown in **Figure 3.14 (d)**.

Although MoS_2-rGO heterostructure shows much better catalytic activity compared to rGO but it does not match the catalytic behaviour of pristine MoS_2 nanoflowers and nanosheets. This could be due to the larger dimensions of rGO compared to MoS_2, which may compromise some of the active sites of MoS_2. We have summarized the

electrocatalytic activity of our prepared samples with other literature reports in **Table 3.1**. The lower value of Tafel slopes and overpotentials of as-synthesized materials in the present work compared to other reports indicates better HER activity of our synthesized electrocatalysts. Among studied materials, MoS_2 nanoflowers shows best electrocatalytic activity for HER, which may be attributed to the availability of defects and exposed edges in well-separated and ordered petals of MoS_2 nanoflowers. Hence, we have indigenously designed electrochemical cell utilizing MoS_2 nanoflowers-based electrodes as cathode for demonstration of hydrogen production, which has been discussed in next section.

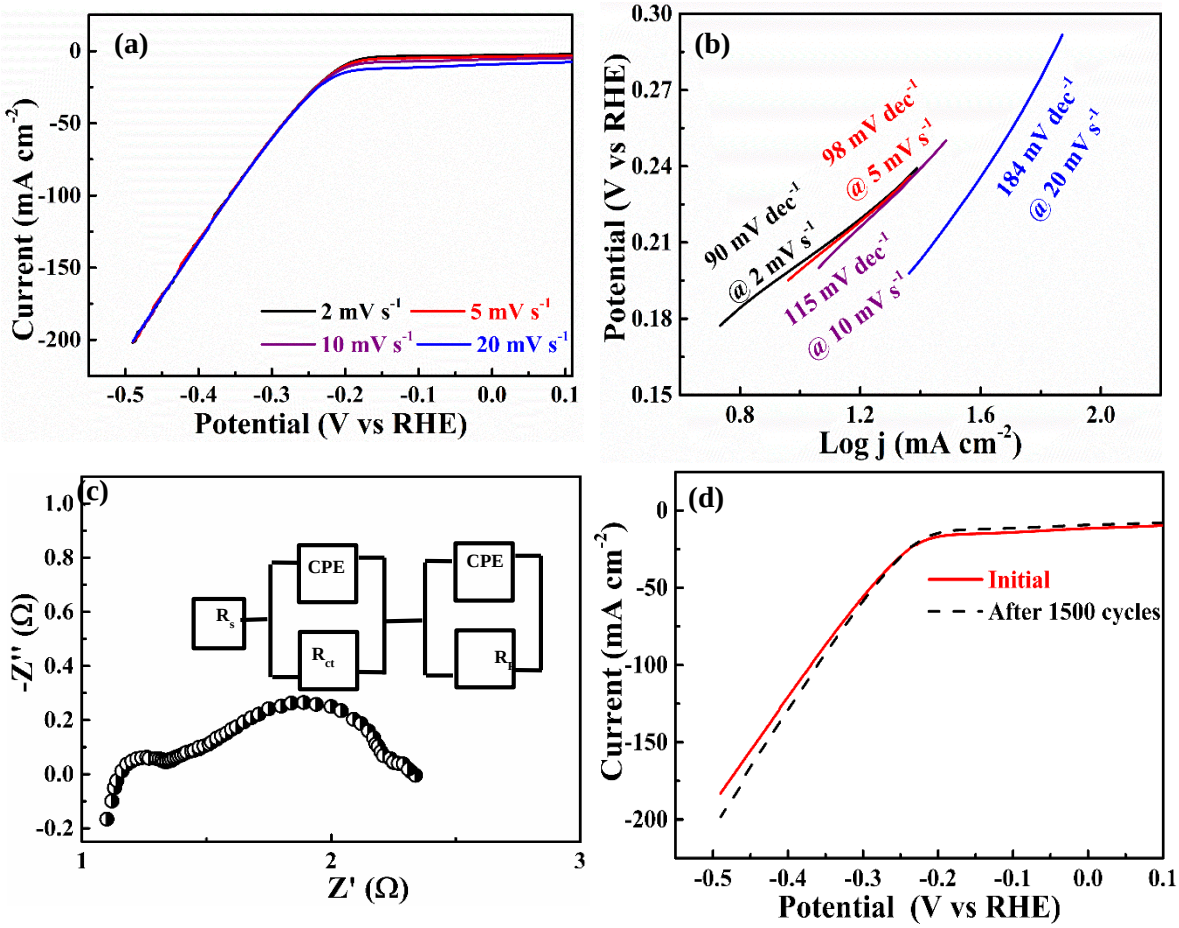

Figure 3.14 *(a) LSV curves at different scan rates, (b) Corresponding Tafel plots, (c) Nyquist plot, and (d) stability test at 20 mV s^{-1} for MoS_2-rGO heterostructure electrodes.*

Table 3.1 The HER Activity of Different MoS_2 Nanostructures.

Catalyst	Tafel Slope (mV dec^{-1})	Electrolyte H_2SO_4	Scan Rate (mV s^{-1})	Overpotential (mV)	Ref.
Sulphur-rich MoS_2	77.7	0.1M	5	255	[186]
Rosette-like MoS_2	71.2	0.5M	2	250	[187]
Vertical MoS_2 Film	75	0.5M	2	-	[141]
Mechanical activated MoS_2	104	0.5M	2	200	[144]
Defect-free MoS_2	87	0.5M	5	265	[139]
Double-gyroid MoS_2	50	0.5M	5	230	[142]
1T/2H MoS_2	61	0.5M	5	225	[168]
2H MoS_2 hollow sphere	74	0.5M	5	250	[188]
MoS_2 nanosheets	68	0.5M	2	226	[77]
Cu doped MoS_2	109	0.5M	2	300	[189]
MoS_2-nanoclusters	123	0.5M	5	212	**Present work**
MoS_2 - nanoflowers	69	0.5M	5	193	**Present work**
2H-MoS_2 nanosheets	115	0.5M	5	198	**Present work**
MoS_2-rGO heterostructure	98	0.5M	5	190	**Present work**

3.3.6 Hydrogen Producing Electrochemical Cell using MoS_2 Nanoflowers as Cathode Material

Among MoS_2 nanostructures, nanoflowers shows the best catalytic behaviour, which may be attributed to its 3D network and arranged petal edges in flower like structure. We have demonstrated hydrogen production and collection using indigenously designed electrochemical cell with 2H-MoS_2 nanoflowers as cathode material.

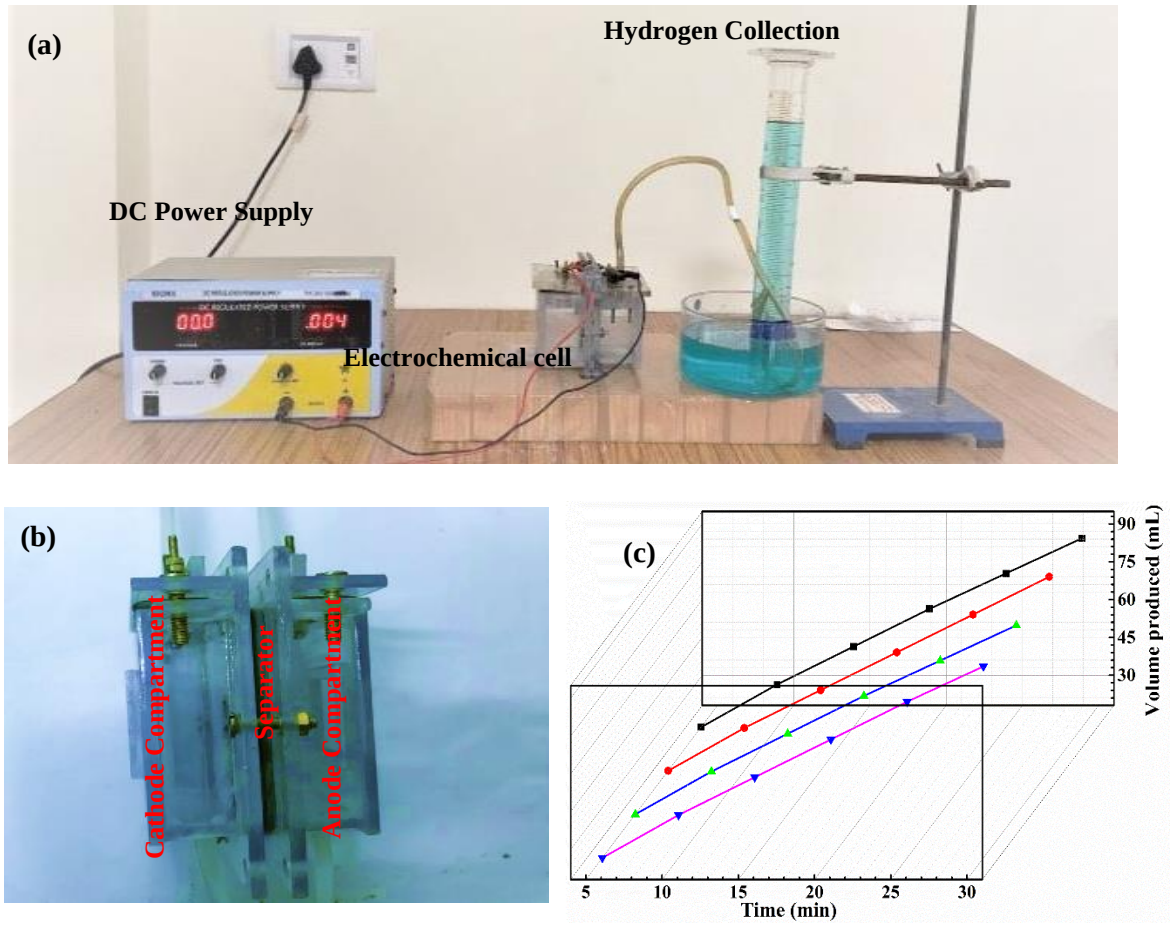

Figure 3.15 *(a) Photograph of hydrogen production and collection unit, (b) Photograph of electrochemical cell and (c) Amount of volume produce in different cycles at 0.2 V.*

Figure 3.15 (a) shows image of full setup of the hydrogen production and collection unit. This work paves the way for developing MoS_2 nanoflowers-based efficient energy generation systems. **Figure 3.15 (b)** shows the hydrogen-producing electrochemical cell where in the cathode chamber MoS_2 nanoflowers coated carbon paper has been used as

cathode and in anode compartment bare carbon paper has been used as anode in indigenously designed electrochemical cell. We have used the 250 mL of acidic electrolyte (0.5 M H_2SO_4) in designed electrochemical cell and tested the designed cell at 0.2 V (near overpotential) for hydrogen production. The generated hydrogen has been collected via water displacement method and the amount of hydrogen produced has been measured in four consecutive cycles, as shown in **Figure 3.15 (c)**, suggesting good repeatability of hydrogen production using a designed electrochemical cell.

3.4 Conclusion

In summary, we have successfully synthesized rGO-HH, rGO-Urea, MoS_2 nanoclusters, MoS_2 nanoflowers, MoS_2 nanosheets and MoS_2-rGO heterostructure via hydrothermal process and examined their electrocatalytic activity for HER. The influence of different morphologies of MoS_2 and its heterostructure with rGO on HER have been investigated in depth in this chapter. The improved catalytic activity for all MoS_2 based samples is observed due to the presence of edge and oxygen functionality. The 2H-MoS_2 nanoflowers shows best catalytic activity in acidic medium among studied materials due to its 3D architecture and higher accessibility of arranged petal's edges. This work identifies the suitable morphologies of MoS_2 nanostructures for HER and based on that study we have demonstrated the production and collection of hydrogen using in-house developed electrochemical cell with 2H-MoS_2 nanoflowers as cathode.